Editors' Suggestion | Featured in Physics

Crack Front Interaction with Self-Emitted Acoustic Waves

D. Massy,[1,4] F. Mazen,[2] D. Landru,[4] N. Ben Mohamed,[4] S. Tardif,[1]
A. Reinhardt,[3] F. Madeira,[2] O. Kononchuk,[4] and F. Rieutord[1]
[1]*Univ. Grenoble Alpes, CEA, INAC-MEM, 38000 Grenoble, France*
[2]*Univ. Grenoble Alpes, CEA, LETI, DTSI, 38000 Grenoble, France*
[3]*Univ. Grenoble Alpes, CEA, LETI, DCOS, 38000 Grenoble, France*
[4]*SOITEC, Parc Technologique des Fontaines, 38190 Bernin, France*

(Received 14 May 2018; published 5 November 2018)

The interaction of a propagating crack in implanted silicon with self-emitted acoustic waves results in periodic patterns on fractured surfaces. Direct measurement of the acoustic emission ahead of the fracture front shows the emergence of dominant acoustic frequency related to the crack velocity. It is shown that the surface modifications are made of roughness modulations due to periodic deviations of the crack front. A physical mechanism explaining the pattern formation is proposed, well in agreement with the observed pattern wavelengths.

DOI: 10.1103/PhysRevLett.121.195501

Dynamic fracture in brittle materials is a complex but crucial problem to understand the mechanisms of material failure. The usual way of describing fast crack dynamics is the linear elastic fracture mechanics (LEFM) [1], in which a singular zone, called the fracture process zone (FPZ), is often defined around the crack tip to embrace all the nonlinear dissipation processes. In this approach, the crack speed v is driven by the balance between the fracture energy Γ needed to create new surfaces and the energy G available at the crack tip. When the latter gets larger, the crack speed asymptotically tends towards the Rayleigh wave speed c_R. However, experiments performed on brittle amorphous materials have shown that this theoretical limit of the velocity is never reached because of crack instabilities [2–4]. Indeed, the branching mechanism appears around $v \sim 0.4c_R$ [5] and crack front destabilization due to nonlinearities at the crack tip arises around $v \sim 0.9c_R$ [6]. These two phenomena have finally been joined within the same description where the transition from a straight crack to microbranching is found to be hysteretic and linked to a finite mode II perturbation at the crack tip [7].

In the case of crystalline materials, the terminal crack velocity reaches high values (0.7–$0.9c_R$) [8–12], essentially because of the presence of cleavage planes, but path instabilities occur at low and high driving forces [13–15].

At the crack tip, the major part of the crack energy is used to separate atomic bonds, but a fraction is also spent in heat generation [16] and acoustic emission [17–19]. The amount of energy corresponding to acoustic emission is quite low, around 1%–5% in PMMA and glass [18,19]. However, the interaction of elastic waves with a fracture front perturbs the crack dynamics. Indeed, stress waves generated during loading or by an ultrasonic transducer have shown to induce crack path instabilities, branching modifications, or speed fluctuations when they run into a crack front [17,20–22]. The Wallner lines, which are circular marks seen on postfracture surfaces, also arise from the interaction of the fracture front with transverse waves emitted at a material discontinuity (defect, sample boundary) [23,24]. More recently, similar features on postfracture surfaces have been shown to come from the interaction of the crack front with localized nonlinear waves propagating along the crack tip (crack front waves) [25,26], even though a controversy arose about the origin of these undulation markings [21,27,28]. Some authors have also used piezoelectric transducers to study the sound emitted by a fast running crack [18,19]. They showed that the signal is first dominated by low frequency components while high frequency components appear at higher velocity. The latest are in fact due to microbranching onset, which is highlighted by the cross-correlation between acoustic emission and surface structure.

These different studies have shown the great importance of acoustic emission when describing crack dynamics, even if the exact impact of self-emitted acoustic waves on the main crack remained quite unclear. In this Letter, we show that crack propagation in implanted silicon generates elastic waves traveling ahead of the crack front at high velocity. By using a dedicated setup, a precise characterization of the acoustic emission allows one to address the fundamental question of the frequency selection mechanism in the crack acoustic emission. After reflection at the sample boundaries, these waves interact with the crack tip and generate highly reproducible periodic patterns on the postfracture surface.

Our experiments have been performed on rectangular silicon samples cut out from a pair of (100) bonded silicon wafers. Such assemblies are common in silicon-on-insulator (SOI) wafer manufacturing using Smart Cut™

technology [29], whose main steps are summarized below. Relatively high doses of light gas ions are implanted in a thermally oxidized monocrystalline silicon substrate which leads to the formation of a buried weakened layer in the crystal. The substrate is then bonded onto a handle wafer using direct wafer bonding [30,31]. Under annealing, the implanted species evolve into microcracks oriented parallel to the (100) surface, and a controlled fracture finally propagates along the implanted layer in a nearly perfect 2D propagation [32,33]. If not thermally, the fracture can be mechanically initiated after applying a certain thermal annealing by inserting a blade between the two wafers. A thin layer of monocrystalline silicon is therefore transferred onto the host substrate, constituting in the end the SOI wafer [Fig. 1(a)].

To monitor the crack propagation, a dedicated optical bench based on infrared transmission in silicon has been developed [33]. The crack is mechanically initiated by a blade which is inserted at the beveled edge of the sample. It has been shown that for homogeneous thermal budget and temperature along the sample, the crack speed rapidly saturates [32]. Higher splitting temperatures lead to higher crack speeds because of increased gas pressure inside the microcavities. Experimentally, fracture initiation at different temperatures is made in a specially designed oven in which the sample is placed during the crack propagation measurement. Figure 1 shows the optical signals (black) recorded for a crack mechanically initiated at 300 °C after a separate annealing dedicated to microcrack development. The time lag between the two intensity drops on the laser signals allows the determination of the crack velocity, which is 2.5 ± 0.1 km s^{-1} in this particular experiment. The following oscillations correspond to laser interferences due to crack opening and can be used to recover the crack deformation profile [33].

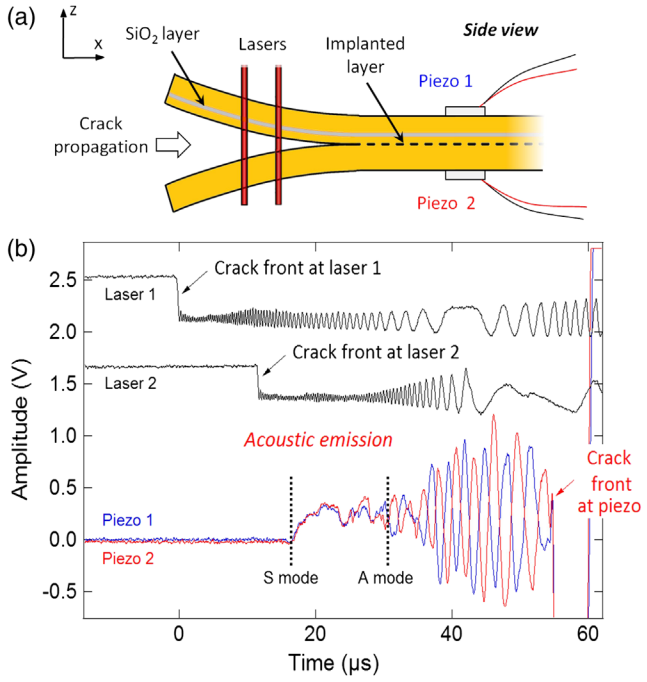

FIG. 1. (a) Crack propagation in implanted silicon. (b) Laser and piezoelectric signals used to monitor the crack propagation and its acoustic emission in a $300 \times 20 \times 1.55$ mm^3 bonded silicon sample with long axis parallel to [100] direction.

To record the acoustic emission of the propagating crack, two 5×5 mm^2 piezoelectric sensors [34] were bonded at the middle of the top and the bottom surfaces. The presence of face-to-face sensors allows the differentiation of symmetric and antisymmetric sample deformations. Typical electrical signals are shown in Fig. 1(b). Two fronts are seen, the first one around $t = 17$ μs (followed by a simultaneous rise of both signals) and the second one at $t = 31$ μs (followed by a remarkable periodic signal in phase opposition). The piezoelectric signals then fall ($t = 53$ μs) and strongly saturate. This corresponds to the arrival time of the crack at the sensor's location, where the divergent movements of the two silicon arms behind the crack front make the sensor saturate and prevent any further acoustic measurement. The signal before this saturation corresponds therefore to the acoustic emission of the propagating crack into the bonded part of the assembly. It is first made of a symmetric deformation (signals in phase) that propagates at high velocity, around 7.5 km s^{-1}. The frequency of the following antisymmetric signal is clearly defined and was measured from the Fourier spectrum of the signal to be equal to 380 kHz. The emergence of this frequency is quite intriguing because the wavelength ($v/f = 6.3$ mm) does not seem to be related to any characteristic length, such as microcrack mean size (10–20 μm) or sample thickness (1.55 mm). In order to investigate the origin of this frequency, the same experiments have been repeated for different crack speeds by changing the fracture temperature. The relationship between measured crack velocity and the piezoelectric signal frequency is shown with red circles in Fig. 2. This evolution can be explained as follows. In the case of a semi-infinite solid, a nondispersive elastic wave known as the Rayleigh wave can propagate at the sample surface [2]. Its penetration in the solid is quite low, about 1 or 2 wavelengths λ. If we now consider a finite solid limited by two plane surfaces at a distance h, two Rayleigh waves are likely to propagate independently at each free surface. However, if the distance h becomes close to λ, the two waves pair up and form symmetric (S_n) or antisymmetric (A_n) Lamb waves [35], where n is the mode number. The dispersion relations of these waves [36] link the frequency ω with the wave vector k, and therefore with the phase and group velocities. The dispersion curves of the fundamental antisymmetric mode A_0 calculated for the studied sample geometry have been plotted in Fig. 2. A remarkable agreement between measured crack propagation speed and A_0 phase velocity for the given frequency is evident.

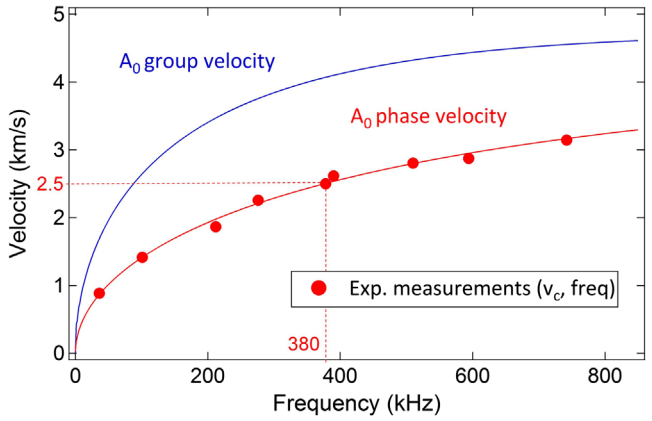

FIG. 2. Experimental evolution of the antisymmetric mode frequency with crack velocity (red circles) and A_0 Lamb mode dispersion curves (solid lines).

During its propagation, the crack emits a wide range of acoustic waves at different frequencies and therefore with different phase velocities v_φ. Among all these waves, the ones propagating with a phase velocity equal to the crack speed (or its projection if the two wave vectors are not collinear) prevail since their amplitudes build up constructively at a given point.

This phenomenon is known as the stationary phase principle and was first described in 1887 by Lord Kelvin to explain the formation of ship wakes [37]. Using standard harmonic waves, the acoustic amplitude a at a point M and time t can be written as

$$a(M,t) = \int_{\substack{M' \in \text{front} \\ t' < t}} \exp[i\phi(M'M, t-t')]\, dr' dt'. \quad (1)$$

The expression for the phase φ and its stationarity depends on the geometry. In our simple quasi-1D case, considering direct harmonic plane waves this expression is simplified:

$$\iint_{(t'<t, M' \in \text{front})} \exp\,[i\phi(M'M, t-t')]\, dt' dr' = \exp i\omega t \int_{(x<d)} \exp ikx\left(1 - \frac{v_\phi}{v_F}\right) dx, \quad (2)$$

where v_F is the crack velocity. It shows that the amplitude will be at maximum if the integrand over all locations of the emitting crack front does not vary, i.e., if $v_\varphi(\omega) = v_F$.

In our case, the crack velocity takes values between 0 and the Rayleigh velocity, which is about 4.9 km s^{-1} in silicon for the (100) surface [38]. According to the dispersion curves for Lamb waves, only one A_0 mode can have a phase velocity in this range of speed, and hence can fulfill the stationary phase condition, and be preferentially excited. This frequency selection through the phase velocity cannot operate for S waves or A modes with order >0, whose phase velocities are always above c_R [39]. Hence, no frequency emerges from the (fast) symmetric signals of Fig. 1(b). Their maximum velocity (around 7.5 km/s) is also in accordance with the fastest S_0 group velocity (see Fig. S1 in Supplemental Material [39]) at small k (compression waves).

The energy of these waves does not propagate at the phase velocity, but at the group velocity v_g. Accordingly, the velocities associated with the occurrence of both symmetric (S_0) and antisymmetric (A_0) signals in Fig. 1(b) are consistent with the group velocities of these two modes. As shown in Fig. 2, the group velocity of the A_0 Lamb mode is higher (typically a factor of 2) than the phase velocity, which explains why acoustic waves are detected ahead of the crack front. This point is of great importance because it gives the opportunity for the acoustic waves to reflect at the sample edges and to come back to interact with the crack front. This interaction leads to roughness surface modifications.

Experimentally, the postfracture surfaces of the silicon samples exhibit a periodic pattern which can be seen on haze maps as shown in Fig. 3. In the case of rectangular samples, the pattern is made of fringes perpendicular to the direction of the fracture front propagation and located at the opposite side of the initiation point. For information, the haze maps are the maps of the intensity of the scattered light from scanning the surface of the sample with a 355 nm laser. The value of the haze is proportional to the square of the surface roughness rms value in the 0.2–5 μm^{-1} spatial frequency range.

To investigate the nature of this pattern, optical interferometer images with an optical resolution of 0.4 μm have been taken at the bright fringe (BF) and dark fringe (DF) locations of the fractured surface. Two examples are shown in Fig. 3, where one can see the postsplit microcrack footprints with typical size around 10 μm. A rms roughness value of 10.7 ± 0.3 Å has been found for DF and

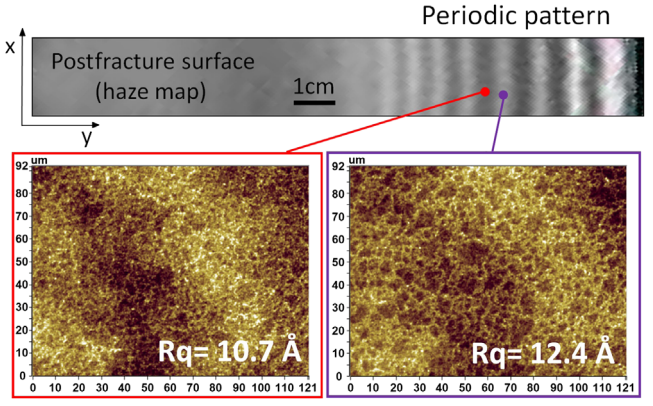

FIG. 3. Haze map of the periodic pattern observed on a postfracture surface (top) and optical interferometer measurements on the host wafer at the bright and dark fringes of the pattern (bottom).

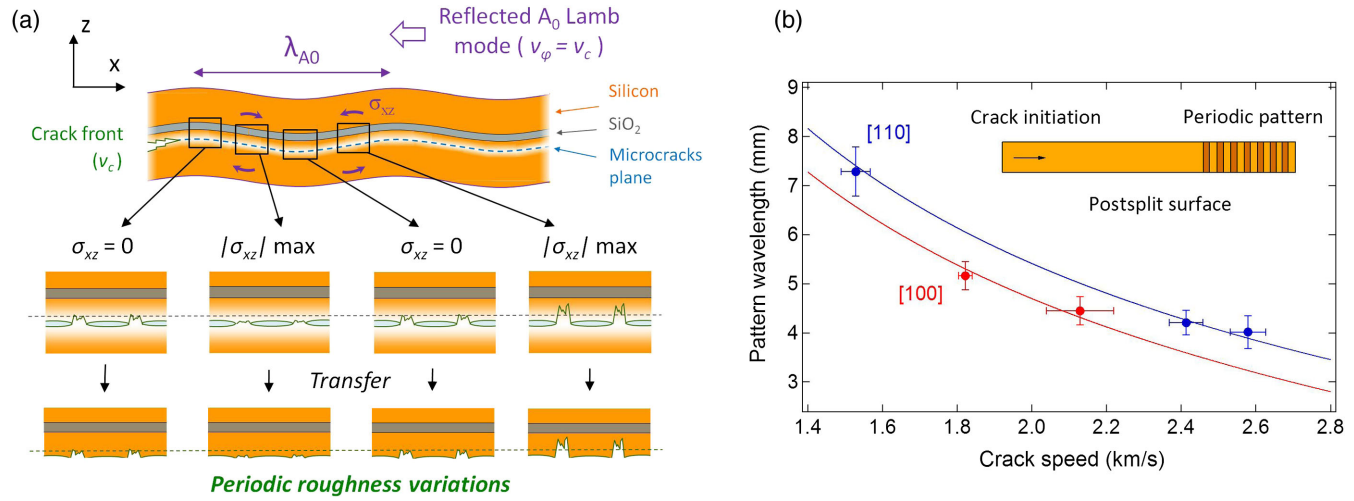

FIG. 4. (a) Interaction between the crack front and the reflected acoustic wave. The A_0 Lamb mode generates bending that leads to crack path deviations between the microcavities and to periodic roughness variations on the postsplit surface. (b) Experimental and theoretical evolution of the pattern wavelength with crack speed.

12.4 ± 0.6 Å for BF. These quantitative measurements confirm the haze data. Moreover, skewness of the height distributions calculated from the interferometer images is positive (0.2 ± 0.04), indicating deviations of fracture crack towards the buried oxide layer of the SOI.

This periodic modulation of the surface roughness is in fact the result of the interaction between the crack front and self-emitted acoustic waves, which have been previously reflected at the sample boundary. Indeed, the gas implantation into the silicon crystal creates platelets which evolve after annealing into microcavities [32]. During the layer transfer, the crack front tends to progress through these open areas to minimize energy dissipation. At the same time, the crack front emits ahead an antisymmetric A_0 Lamb mode which generates local shear stresses into the wafer. In our strip samples, the acoustic waves propagate along the same axis as the crack front, which means that the A_0 Lamb mode excited in our conditions has a phase velocity equal to the crack speed (Fig. 2). Since the group velocity of the A_0 Lamb mode is higher than the phase velocity, the acoustic deformation propagates ahead of the crack front, reflects at the sample edge, and comes back to interact with the crack. Then, due to the local stress field induced by the A_0 Lamb mode at the time of the interaction (shear stress, mode II), the crack tip is more or less deviated between the microcavities, leading in the end to roughness variations at large scale as is outlined in Fig. 4(a). Note that even with no external stress ($\sigma_{xy} = 0$) the crack front deviation always occurs on the buried oxide side since the lower oxide elastic modulus allows more efficient stress relaxation than silicon. The shear stress induced by the A_0 mode (σ_{xz} component) modulates these path deviations.

The pattern wavelength seen on the silicon postfracture surfaces can then be linked to the acoustic emission frequency using the same stationary phase argument, considering the time at which the crack reaches the observation point $M(d,t)$. In Eq. (1), taking into account waves reflected at the edge ($x = L$) of the wafers,

$$\iint_{(t'<t, M' \in \text{front})} \exp[i\phi(M'M, t-t')]\, dt'\, dr'$$
$$= \exp ik2(L-d) \int_{(x<d)} \exp ik(d-x)\left(1 - \frac{v_\phi}{v_F}\right) dx. \quad (3)$$

It means that the pattern wavelength is simply equal to half of the A_0 mode wavelength. To check this, similar experiments have been performed with silicon samples cut in the [110] or the [100] direction. The evolution of the pattern wavelength with the crack speed (points) is compared to the evolution of the calculated half wavelength (lines) of the corresponding A_0 mode [Fig. 4(b)]. The agreement between these data validates, therefore, the mechanism proposed above. The changes in wavelength with crystallographic directions are due to variations of elastic constants leading to different Lamb wave velocities.

In conclusion, we showed that the acoustic emission of a propagating crack has a significant impact on its propagation path. The acoustic waves are selected by the crack speed ($v_\varphi = v_F$) and the sample geometry (Lamb waves for plates) via phase stationarity arguments. In the case of a crack running parallel to the surface of silicon slab, the flexural waves (antisymmetric A_0 Lamb mode) are excited preferentially and generate bending and shear stress in the sample. Since its group velocity is higher than its phase velocity, the A_0 mode propagates ahead of the crack front, reflects at the sample's edges, and comes back to interact with the crack tip. The shear stress field of these waves leads to crack path deviations at large scale and generates periodic patterns made of roughness modulations on the postfracture surface. The accurate agreement between the

experimental pattern wavelengths and the associated crack velocities in the case of rectangular samples confirms this mechanism. These results may provide new views to interpret the formation of periodic surface marks on fracture surfaces [40], often interpreted with a close concept of "front waves." The higher thicknesses, more complex fracture geometries, and propagation paths used in these experiments may be a reason why the wave selection is less clear in these experiments.

We would like to acknowledge support from the European Union authorities through the ECSEL-OCEAN 12 program.

[1] L. B. Freund, *Dynamic Fracture Mechanics* (Cambridge University Press, Cambridge, England, 1990).
[2] K. Ravi-Chandar, *Dynamic Fracture* (Elsevier, Oxford, 2004).
[3] J. Fineberg, S. P. Gross, M. Marder, and H. L. Swinney, Phys. Rev. Lett. **67**, 457 (1991).
[4] A. Livne, O. Ben-David, and J. Fineberg, Phys. Rev. Lett. **98**, 124301 (2007).
[5] E. Sharon, S. P. Gross, and J. Fineberg, Phys. Rev. Lett. **74**, 5096 (1995).
[6] T. Goldman, R. Harpaz, E. Bouchbinder, and J. Fineberg, Phys. Rev. Lett. **108**, 104303 (2012).
[7] T. G. Boué, G. Cohen, and J. Fineberg, Phys. Rev. Lett. **114**, 054301 (2015).
[8] J. J. Gilman, J. Appl. Phys. **27**, 1262 (1956).
[9] D. Hull and P. Beardmore, Int. J. Fract. Mech. **2**, 468 (1966).
[10] J. H. Greenwood, J. Mater. Sci. **6**, 390 (1971).
[11] T. Cramer, A. Wanner, and P. Gumbsch, Phys. Status Solidi A **164**, R5 (1997).
[12] J. A. Hauch, D. Holland, M. P. Marder, and H. L. Swinney, Phys. Rev. Lett. **82**, 3823 (1999).
[13] T. Cramer, A. Wanner, and P. Gumbsch, Phys. Rev. Lett. **85**, 788 (2000).
[14] J. R. Kermode, T. Albaret, D. Sherman, N. Bernstein, P. Gumbsch, M. C. Payne, G. Csányi, and A. De Vita, Nature (London) **455**, 1224 (2008).
[15] D. Sherman, M. Markovitz, and O. Barkai, J. Mech. Phys. Solids **56**, 376 (2008).
[16] W. Döll, Polym. Eng. Sci. **24**, 798 (1984).
[17] K. Ravi-Chandar and W. G. Knauss, Int. J. Fract. **26**, 189 (1984).
[18] S. P. Gross, J. Fineberg, M. Marder, W. D. McCormick, and H. L. Swinney, Phys. Rev. Lett. **71**, 3162 (1993).
[19] J. F. Boudet, S. Ciliberto, and V. Steinberg, Europhys. Lett. **30**, 337 (1995).
[20] J. Fineberg, S. P. Gross, M. Marder, and H. L. Swinney, Phys. Rev. B **45**, 5146 (1992).
[21] D. Bonamy and K. Ravi-Chandar, Phys. Rev. Lett. **91**, 235502 (2003).
[22] J. F. Boudet and S. Ciliberto, Phys. Rev. Lett. **80**, 341 (1998).
[23] H. Wallner, Z. Phys. **114**, 368 (1939).
[24] D. Hull, *Fractography: Observing, Measuring and Interpreting Fracture Surface Topography* (Cambridge University Press, Cambridge, England, 1999).
[25] E. Sharon, G. Cohen, and J. Fineberg, Nature (London) **410**, 68 (2001).
[26] E. Bouchaud, J. P. Bouchaud, D. S. Fisher, S. Ramanathan, and J. R. Rice, J. Mech. Phys. Solids **50**, 1703 (2002).
[27] E. Sharon, G. Cohen, and J. Fineberg, Phys. Rev. Lett. **93**, 099601 (2004).
[28] D. Bonamy and K. Ravi-Chandar, Phys. Rev. Lett. **93**, 099602 (2004).
[29] M. Bruel, Electron. Lett. **31**, 1201 (1995).
[30] H. Moriceau, F. Rieutord, F. Fournel, Y. L. Tiec, L. D. Cioccio, C. Morales, A. M. Charvet, and C. Deguet, Adv. Nat. Sci. Nanosci. Nanotechnol. **1**, 043004 (2010).
[31] F. Rieutord, B. Bataillou, and H. Moriceau, Phys. Rev. Lett. **94**, 236101 (2005).
[32] J. D. Penot, D. Massy, F. Rieutord, F. Mazen, S. Reboh, F. Madeira, L. Capello, D. Landru, and O. Kononchuk, J. Appl. Phys. **114**, 123513 (2013).
[33] D. Massy, F. Mazen, S. Tardif, J. D. Penot, J. Ragani, F. Madeira, D. Landru, O. Kononchuk, and F. Rieutord, Appl. Phys. Lett. **107**, 092102 (2015).
[34] Wideband Piezoelectric Sensors ref Z05T5X5SSYXC6 from Fuji Ceramics, Japan; V. Giurgiutiu and A. N. Zagrai, J. Intell. Mater. Syst. Struct. **11**, 959 (2000).
[35] H. Lamb, Proc. R. Soc. London Math. Phys. Eng. Sci. **93**, 114 (1917).
[36] K. F. Graff, *Wave Motion in Elastic Solids* (Dover, New York, 1991).
[37] R. S. Johnson, *A Modern Introduction to the Mathematical Theory of Water Waves* (Cambridge University Press, Cambridge, England, 1997).
[38] H. Coufal, K. Meyer, R. Grygier, P. Hess, and A. Neubrandt, J. Acoust. Soc. Am. **95**, 1158 (1994).
[39] See Supplemental Material at http://link.aps.org/supplemental/10.1103/PhysRevLett.121.195501 for group and phase velocity calculations of the different Lamb modes.
[40] L. Zhao, D. Bardel, A. Maynadier, and D. Nelias, Nat. Commun. **9**, 1298 (2018).